



Numerical analysis of the compressive and shear failure behavior of rock containing multi-intermittent joints



Xiang Fan ^{a,d}, Hang Lin ^{b,*}, Hongpeng Lai ^a, Rihong Cao ^b, Jie Liu ^c

^a School of Highway, Chang'an University, Xi'an, Shannxi, 710064, China

^b School of Resources and Safety Engineering, Central South University, Changsha, Hunan, 410083, China

^c Department of Building Engineering, Hunan Institute of Engineering, Xiangtan 411104, China

^d Engineering Research Center of Catastrophic Prophylaxis and Treatment of Road & Traffic Safety of Ministry of Education, Changsha University of Science & Technology, Changsha, Hunan, 410114, China

ARTICLE INFO

Article history:

Received 23 August 2018

Accepted 1 November 2018

Available online 27 December 2018

Keywords:

Direct shear test

Intermittent joint

Failure behavior

Contact force evolution

Particle flow code

ABSTRACT

The failure behavior of intermittent jointed rocks is dependent on joint configurations. Joint inclination angle and continuity factor determined the joint arrangement in a rectangular numerical sample that was established by using the particle flow code approach. To identify the differences in the failure processes of identical intermittent jointed samples, uniaxial compressive and shear loads were applied on each sample. The crack growth path presented the four typical crack coalescence patterns identified via compressive and shear numerical tests. The crack coalescence pattern was associated with joint slant angle and continuity factor. The observed crack coalescence patterns of every sample with the same inclination angle and continuity factor were partially identical under compressive and shear loading. The differences in the crack patterns of the compressive and shear failure processes were described and compared. Typical compressive and shear failure processes were illustrated. Four compressive and three shear failure modes were identified. The cracking location and number of cracks in each failure mode were different. Additionally, the contact force evolution among particles during shear and compressive loading was different and likely accounted for the differences in cracking patterns. Under compressive or shear loading, the contact force concentration in each sample underwent the following stages: uniform distribution before loading, concentrated distribution, and scattered distribution after failure.

© 2018 Académie des sciences. Published by Elsevier Masson SAS. All rights reserved.

1. Introduction

A natural rock mass is divided into rock blocks by various discontinuities, such as joints, bedding planes, and cleavages. Therefore, a rock mass is a nonhomogeneous, anisotropic engineering geological body. The construction of tunnels, oil reservoirs, and nuclear waste storage caverns within weak rock masses encounters numerous engineering problems, such as rock falls, fissure water, and collapse. Given that discontinuities affect the stability of engineering structures, the mechanical behaviors of jointed rocks must be properly evaluated. Thus, numerous studies have been conducted to understand

* Corresponding author.

E-mail addresses: 279294111@qq.com (X. Fan), linhangabc@126.com (H. Lin), laihp168@chd.edu.cn (H. Lai), 18229997417@163.com (R. Cao), ljydsjlj@163.com (J. Liu).

<https://doi.org/10.1016/j.crme.2018.11.001>

1631-0721/© 2018 Académie des sciences. Published by Elsevier Masson SAS. All rights reserved.

the failure behaviors of fractured rocks or rock-like materials [1–6]. The mechanical behavior of jointed rocks depends on joint arrangements within samples. Joints randomly exist within natural rock masses. Therefore, the values of joint sets, lengths, and slant angles are difficult to determine in natural rock masses. Moreover, the mechanical behavior and rupture mechanism of rock masses are very complicated. Joint lengths, inclination angles, and sets are the most important factors that influence the mechanical behavior of fractured rocks. In the published reports [7–11], joint distribution is idealized to explore the relationship between joint geometries and strength, deformation, or failure mode. Moreover, the various combinations of joint inclination angles and joint sets could be carefully considered using synthetic samples. The greatest advantage of a synthetic rock-like sample is the introduction of desired flaws into the sample. Rock-like materials, like plaster and cement, are popularly used to cast artificial rock samples given the similarity of their brittle properties with those of natural rocks [12–16]. Two or three flaws could be pre-fabricated during the casting of rock-like samples. Over the past decades, many innovative methods have been developed to create open flaws, such as the insertion of a thin iron sheet, mica, or paper, into the cast rock [9,10,12,13].

The influence of the joint inclination angle on compressive strength and cracking and the ratio of flaw length to sample size on cracking has been experimentally or numerically investigated [17–20]. With the development of hydraulic cutting technology, natural rocks could be prepared as prismatic or cylindrical samples, and then flaws are incised as planned by using a hydraulic cutter [21]. Flaw creation, done either through the insertion of a thin sheet or hydraulic cutting, crack initiation, propagation, and coalescence, are influenced by flaw configuration [22–25]. In experimental and numerical studies, cracking has been classified as shear, tensile, and wing cracks. Different cracking paths create various types of crack coalescence patterns. When two or three flaws are arranged within samples, crack coalescence patterns are simple relative to those in multi-jointed samples. Multi-jointed blocks are prepared to explore complicated cracking types and failure modes under uniaxial, biaxial, or triaxial loading condition [26–30]. Physical laboratory tests allow direct visual evaluation but often encounter discreteness in strength and manufacturer's error and cannot measure internal stress. To overcome the disadvantages of laboratory tests, numerical approaches, including the distinct element method (DEM), have been developed to study fractured samples under compressive or shear loading [31–37]. DEM is used to complement physical tests. Using the particle flow code (PFC) approach, Zhang and Wong [38] measured stress distributions around an open flaw under uniaxial compression. Stress distribution is difficult to measure by using physical tests. Cao et al. [34] also established a multi-jointed bonded particle model to repeat the cracking process in physical tests and summarized the crack coalescence types.

A jointed rock is subjected not only to compressive stress but also to shear stress. The shear strength of a rock joint or a jointed rock is considerably lower than compressive strength. Thus, failure more easily occurs under shear load than under compressive load. Previous studies have revealed that the shear strength of continuous joints is related to joint surface roughness [39–43]. However, the factors that influence the shear behavior of intermittent joints are different from those that influence continuous joints. An intermittent joint can be classified as coplanar and non-coplanar based on shear direction. The shear strength and failure of intermittent joints are different [44,45]. The shear failure behavior of non-coplanar joints depends on the joint configurations and sets along the shear direction and the angle from the shear direction to the joints. In addition, cracks occur at joint tips, grow and finally coalesce with adjacent joint tips. To avoid bending moments, a normal load is applied on intermittent joints during shear loading. This process is similar to the shear test of continuous rock joints. However, normal stress exerts less influence on the shear strength of intermittent joints than on continuous rock joints. Experimental results show that shear strength strongly depends on joint space and orientation [45]. To investigate cracking under shear load, short flaws are arranged along the central shear axis. Gehle and Kutter [46] reported that initial crack orientation and normal stress are the most important parameters that influence the shear behavior of intermittent joints. The whole shear process comprises three basic phases, as identified by Gehle and Kutter [46]. Zhang et al. [47] and Liu et al. [48] utilized the Realistic Failure Process Analysis (RFPA) and PFC to establish a jointed model that contained several non-persistent joints with changing slant angle along the shear plane, respectively. Moreover, crack initiation and propagation under shear load were modeled.

As described above, joint geometries significantly influence the strength, deformation, and failure of jointed rocks. In addition, different loading methods cause different failure processes. In this study, PFC was used to construct jointed numerical specimens that contained multi-non-persistent joints. Shear and compressive loads were applied on numerical samples to identify differences among crack propagation, coalescence, and failure mode.

2. Establishment of numerical model

2.1. Joint configuration

In reference to Chen's work [9], prismatic sample sizes were determined as 150 mm × 150 mm × 25 mm (length × height × width). Two geometrical parameters, joint inclination angle α and joint continuity factor k , were used to determine joint configurations. As shown in Fig. 1a, the origins of coordinates $x_1 o y_1$ and $x_2 o y_2$ were centered in the samples. The joint inclination angle was measured from the positive x -axis to the joint plane. The joint continuity factor was defined as the ratio of the total length of all joints on the same joint plane to the length of joint plane located within the sample. Fig. 1a shows an initial joint plane parallel to the x_1 -axis, i.e. $\alpha = 0^\circ$. The distance between two adjacent joint planes or two midpoints of any two adjacent joints on the same joint plane is maintained at 3 cm. The distance is represented using d as shown in Fig. 1.

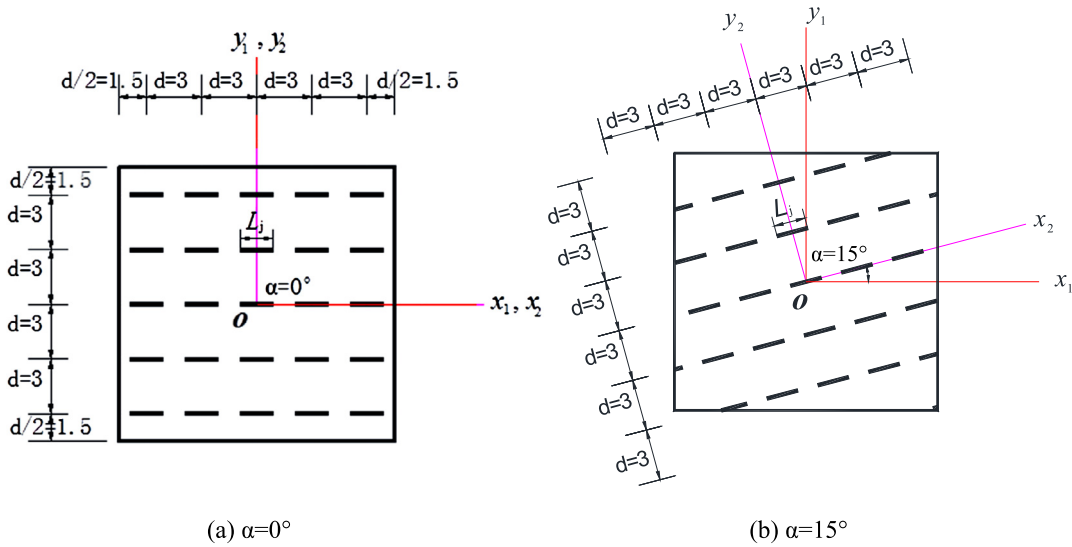


Fig. 1. Illustration of the joint system [35].

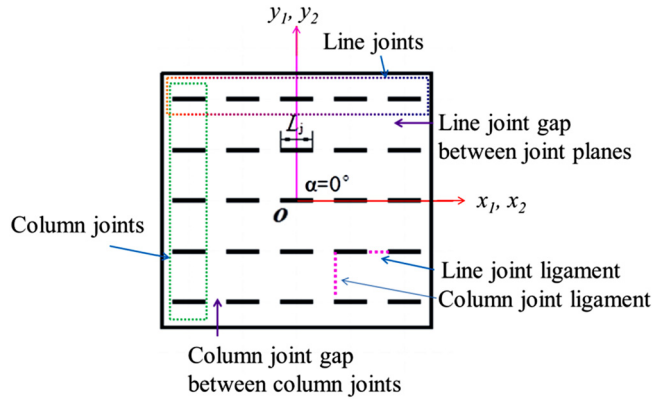


Fig. 2. Illustration of the detailed joint configuration within the sample.

The midpoint of the central joint always corresponded to the origin of the coordinates and to the sample's center. To create more slant joints, the $x_1 o y_1$ and $x_2 o y_2$ coordinates were rotated in a counterclockwise direction at an interval of 15° to obtain joint inclination angles of $15^\circ, 30^\circ, 45^\circ, 60^\circ, 75^\circ,$ and 90° . Fig. 1b shows the case where $\alpha = 15^\circ$. The joint continuity factor was set at 0.4, 0.6, and 0.8. The complete joint length L_j for $k = 0.4, 0.6,$ and 0.8 was 12 mm, 18 mm, and 24 mm, respectively. Note that in the cases where $\alpha = 15^\circ, 30^\circ, 60^\circ,$ and 75° , even if the joint inclination angle was kept constant, joints that intersected the sample edge were left incomplete, i.e. these joints were partly located outside the sample. Each sample was designated by the combination of the slant angle and the continuity factor, α and k . For example, 0-0.4 represents the sample with $\alpha = 0^\circ$ and $k = 0.4$.

To better understand the failure behavior of the jointed model, the joints inside the sample are described in detail. As shown in Fig. 2, the joints located on the same joint plane in the x -direction were called line joints, whereas those located in the y -direction were called column joints. The gap between line joint planes was the line joint gap and that between column joints was the column joint gap. The connecting part between adjacent line joints was called the line joint ligament, whereas that between the column joints was called the column joint ligament.

2.2. Compressive and shear models

In this study, a parallel bond was used to create bonded particle models. Micro-parameter values were determined via a trial-and-error process. Based on the obtained mechanical parameters in a physical test [35], when the micro-parameter values listed in Table 1 were adopted in the bonded particle model, the uniaxial compressive strength and elastic modulus were approximately equivalent to those in Table 2. Thus, the intact numerical model that was established by adopting the values listed in Table 1 was further used to construct the jointed model. The bonded particle model consisted of 60,412 particles. Based on the joint system described in Section 2.1, smooth-joint contact was adopted to the created joints. Further

Table 1

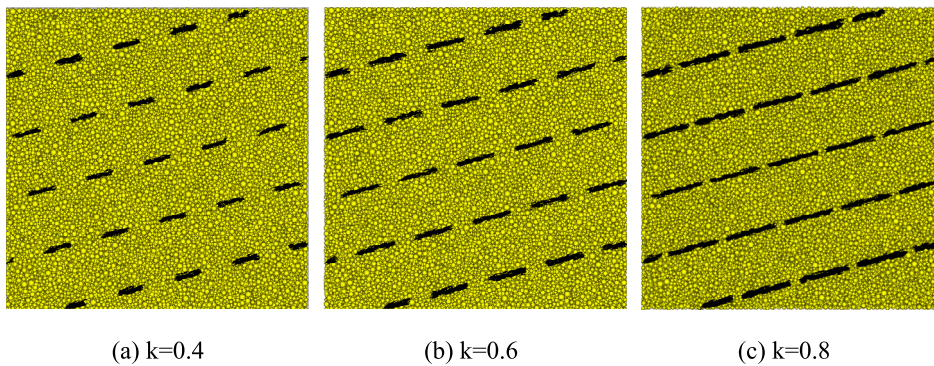
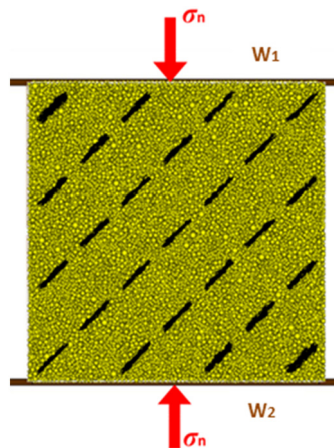
Micro-parameters adopted in the numerical model.

Minimum radius (mm)	0.85
Radius multiplier	1.66
Density (kg/m ³)	1158.4
Particle friction coefficient	0.5
Contact Young's modulus (GPa)	4.2
Ratio of normal to shear stiffness, k_n/k_s	2.5
Normal bond strength (MPa)	6.2
Standard deviation of normal bond strength (MPa)	1.24
Shear bond strength (MPa)	10.0
Standard deviation of shear bond strength (MPa)	2.0

Table 2

Experimental and numerical results for intact sample [35].

	Experimental results	Numerical results
Uniaxial compressive strength, σ_p (MPa)	8.27	8.24
Young's modulus, E (GPa)	4.04	4.01

**Fig. 3.** Numerical jointed models ($\alpha = 15^\circ$).**Fig. 4.** Uniaxial compressive model.

details regarding the smooth joint are discussed in the PFC user's manual [49]. The established jointed models are partly shown in Fig. 4. In the numerical models, bolded black lines represented the joints. As mentioned in Section 2.1, joint lengths varied in accordance with different continuity factors; meanwhile, the length of the line joint ligament changed with the value of k .

The uniaxial compressive test (UCT) and direct shear test (DST) were performed using the same numerical jointed model. In the uniaxial numerical test shown in Fig. 3, compressive loading was applied by moving rigid walls (W_1 and W_2). This loading pattern corresponded to the loading platens of a servo-control machine. In the shear numerical test, W_5 and W_6

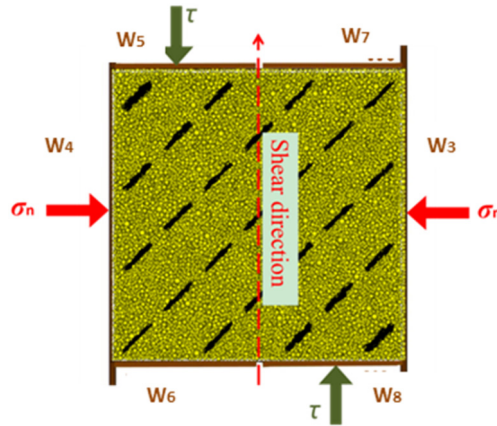


Fig. 5. Direct shear model.

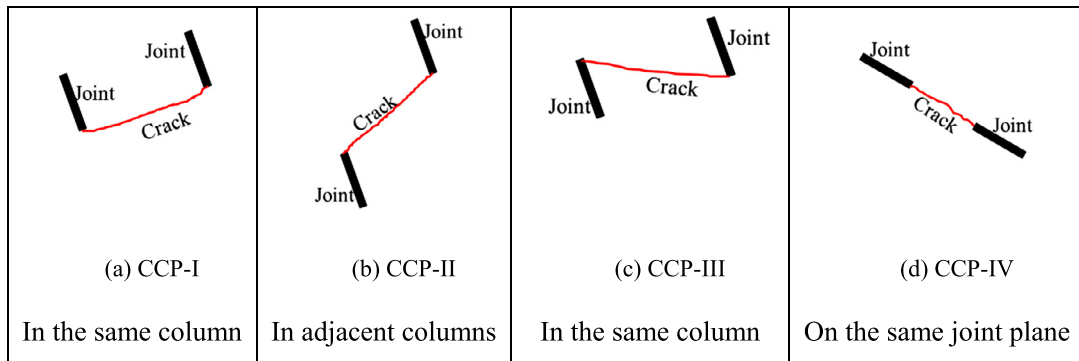


Fig. 6. Crack coalescence patterns.

were kept constant, whereas W_7 and W_8 were moved in the shear direction under a normal stress (σ_n) of 0.5 MPa. The shear direction coincided with the compressive loading direction for the comparison of the failure process.

3. Failure characteristics

3.1. Crack coalescence

The crack growth path, which creates various crack coalescence patterns (CCP), is affected by the joint inclination angle, the continuity factor, and the loading direction. This study evidenced that cracks initiated at the joint tip in both compressive and shear simulations and then propagated toward the tip of the adjacent joint in the same column or on the same joint plane. The cracking path was carefully considered. However, the joint length and inclination angle were ignored during the identification of crack coalescence patterns due to variations in slant inclinations. Finally, four typical coalescence patterns were identified based on the crack growth path in numerical compressive and shear tests, as shown in Fig. 6.

CCP-I: in the same joint column, the crack initiates at the joint tip, then vertically propagates toward another joint tip located on the same side, and finally coalesces, as shown in Fig. 6a.

CCP-II: in two adjacent joint columns, the crack initiates at the joint tip, then propagates toward another joint tip located in an adjacent column on a different joint plane, and finally coalesces, as shown in Fig. 6b.

CCP-III: in the same joint column, the crack initiates at the joint tip, then transversely propagates toward another joint tip on the other side, and finally coalesces, as shown in Fig. 6c.

CCP-IV: On the same joint plane, the crack initiates at the joint tip and then propagates toward the adjacent joint tip on the same plane, as shown in Fig. 6d.

Among the four observed crack coalescence patterns, CCP-I and CCP-II occurred in the same joint column, CCP-II in two adjacent joint columns, and CCP-IV on the same joint plane. At the same k value, CCP-II and CCP-III passed through a growth path that was longer than those of CCP-I and CCP-IV. The four crack coalescence patterns observed under compressive and shear loading are summarized in Table 3. Some cracks did not coalesce prior to peak strength but during residual stage; thus, the crack coalescence patterns of each sample are summarized before axial or shear stress reached the residual moment of the compressive stress–strain or shear stress–shear displacement curve. This phenomenon is called initial residual stage.

Table 3
Summary of crack coalescence patterns in compressive and shear tests.

Sample ID	UCT				DST			
	CCP-I	CCP-II	CCP-III	CCP-IV	CCP-I	CCP-II	CCP-III	CCP-IV
0-0.4	*	*					*	
0-0.6	*	*					*	
0-0.8	*	*				*		*
15-0.4	*	*				*		
15-0.6	*	*			*	*		
15-0.8	*	*			*			
30-0.4	*	*	*		*	*	*	
30-0.6	*	*	*		*	*		
30-0.8	*	*			*			
45-0.4			*	*		*		
45-0.6				*		*		
45-0.8				*	*	*		
60-0.4				*		*		
60-0.6				*		*		
60-0.8				*	*			
75-0.4				*		*	*	
75-0.6				*		*		*
75-0.8				*				*
90-0.4				*				*
90-0.6				*				*
90-0.8				*				*

The results of the compressive test indicated that the crack coalescence pattern is related to the joint inclination angle. The crack coalescence patterns were similar for samples with the same α . When $\alpha = 0^\circ$, 15° , and 30° , CCP-I and CCP-II were the main joint-connecting types. CCP-III was observed in a few samples, including 30-0.4, 30-0.6, and 45-0.4. CCP-IV was observed only in samples with higher inclination angles of 45° to 90° . In the shear test, CCP-I and CCP-II were mainly observed in samples with inclination angles of 15° to 75° . CCP-III occurred in the failure process of 0° , 30° , and 75° samples. CCP-IV occurred in 90° samples, as well as in samples 0-0.8 and 75-0.8. Sample 0-0.8 was an exception. Given that the line joint ligament of this sample was only 6 mm, the crack run through the line joint ligament easily under accessional compressive stress from the shear-loading wall. As a matter of fact, crack coalescence is influenced by the loading direction. CCP-IV occurred when the joint inclination angle from the loading direction to the joint plane was small, for example, in 90° samples. The relative location between the joint and shear plane significantly influences the cracking path. CCP-III and CCP-IV occurred when joints were regularly arranged on the joint plane, such as in 45° and 90° samples. As summarized in Table 3, most samples exhibited one or two crack coalescence patterns; however, some samples exhibited all three patterns. For one sample with the same α and k values, such as 15° , 30° , and 90° samples, identical crack coalescence patterns were observed under compressive and shear loading. Additionally, due to the loading difference, a completely different cracking path occurred in 45° and 60° samples. Although different loadings may create various crack coalescence patterns, the crack coalescence pattern is generally the same for samples with identical inclination angles, except for sample 45-0.4.

3.2. Compressive failure process

As described above, the crack propagation path and coalescence were dependent on the joint configurations. To describe the typical compressive failure processes, four samples were selected based on their crack propagation and coalescence patterns. In the compressive test of jointed rocks, cracking was not obvious during the early stage of loading. Therefore, the failure process close to peak uniaxial stress (σ_p) was carefully considered. Three critical rupturing moments, $0.9\sigma_p$, σ_p , and initial residual, represented the failure process. Each rupturing moment that corresponded to the axial stress was marked on the compressive stress–strain curve with A ($0.9\sigma_p$), B (σ_p), and C (initial residual moment). The axial stress of each sample was normalized to improve the comparison between samples.

In the bonded particle model, when the local stress applying on the parallel bond exceeds the shear bond strength in the shear direction or the normal bond strength in the normal direction, the parallel bond ruptures. The shear and normal bond strength are pre-determined during the establishment of the numerical model. Each bond rupture creates one micro-crack. The location of the ruptured parallel bond is marked in red color. The majority of the micro-cracks form macro-cracks. Fig. 7 shows the compressive failure of sample 0-0.6. Referring to Fig. 7a, at $0.9\sigma_p$, the micro-cracks were scattered throughout the gaps of the column joints. This finding demonstrated that particle bonds began rupturing. However, cracking was inconspicuous. Comparing Fig. 7c with Fig. 7b revealed that cracks dramatically developed from $0.9\sigma_p$ to σ_p . Therefore, at σ_p , cracks initiated at joint tips and propagated in the direction perpendicular to the line joint plane. Axial stress reached the peak value, but few connecting joints, which meant that the neighbor joints were connected by crack, were present. As loading continued after σ_p , more cracks distinctly coalesced, in a fashion similar to CCP-I and CCP-II, as shown in Fig. 7d. Comparing Fig. 7c with Fig. 7d showed that the crack quickly coalesced from σ_p to the initial residual

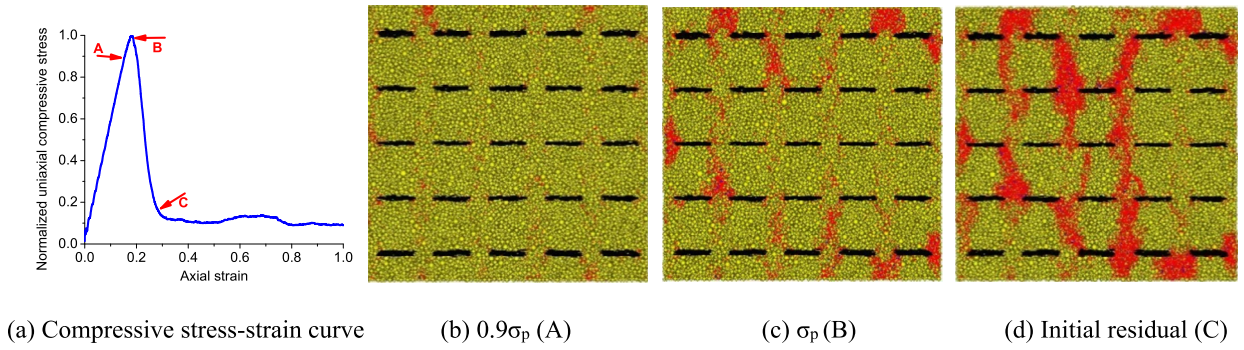


Fig. 7. Compressive failure process for sample 0-0.6.

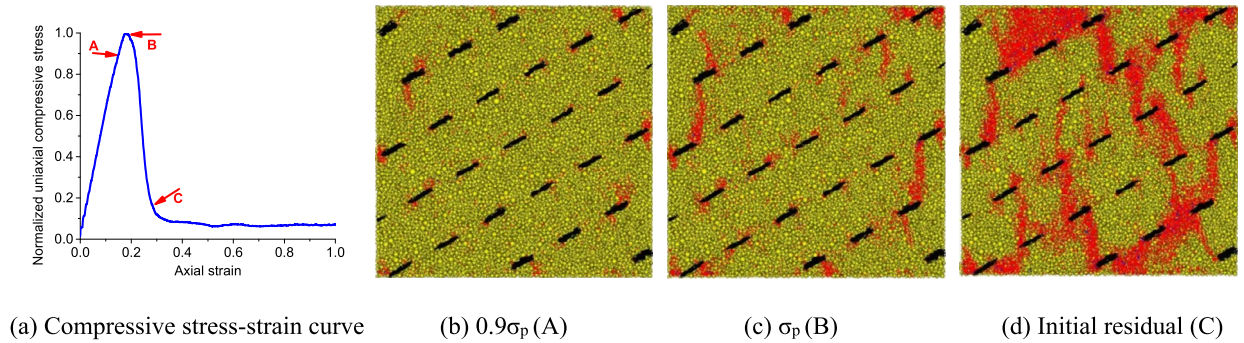


Fig. 8. Compressive failure process for sample 30-0.4.

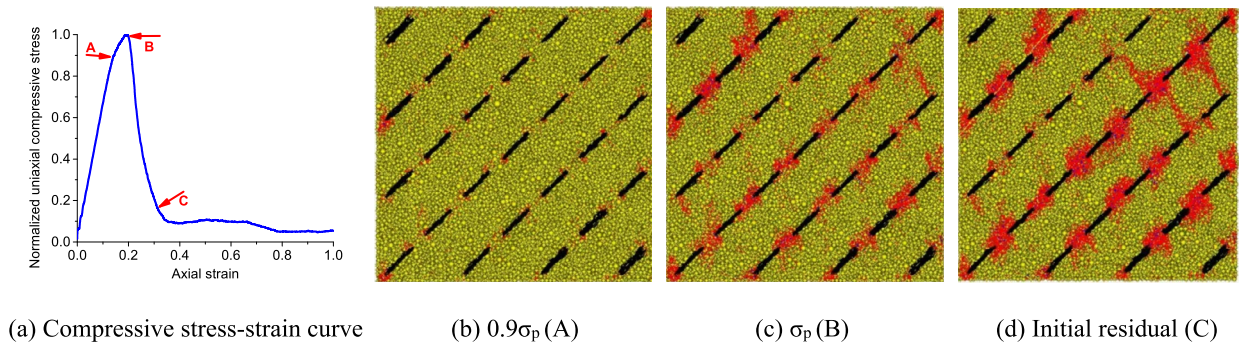


Fig. 9. Compressive failure process for sample 45-0.6.

moment. However, crack coalescence was seldom observed before σ_p . Fig. 7 shows that cracks finally coalesced in the column joint gaps. The failure mode illustrated by sample 0-0.6 is called vertical cleavage failure (compressive failure mode I, CFM-I) and was observed only in 0° samples. In this failure mode, cracks finally ran through the samples in the vertical direction if the load continued in the residual stage.

Fig. 8 shows the compressive failure process of sample 30-0.4. Combining the compressive stress–strain curve (Fig. 8a) at $0.9\sigma_p$, cracks initiated at one tip of the joint, whereas some initiated at both joint tips, as shown in Fig. 8b. Crack initiation was more noticeable than that shown in Fig. 7b. At σ_p , cracks continued to initiate and propagate, and several cracks coalesced from $0.9\sigma_p$ to σ_p , as shown in Fig. 8c. After peak strength, crack coalescence continued to develop, as shown in Fig. 8d. CCP-I, CCP-II, and CCP-III were observed throughout the whole cracking process. CCP-II and CCP-III were the main crack coalescence types. The failure process illustrated in Fig. 8 is called slant cleavage failure (compressive failure mode II, CFM-II) and was mainly observed in 15° and 30° samples and in sample 45-0.4.

Fig. 9 shows the compressive failure of sample 45-0.6. Combining the compressive stress–strain curve (Fig. 9a), at $0.9\sigma_p$, micro-cracks were concentrated at joint tips. At σ_p , more micro-cracks were mainly located at the line joint ligaments; moreover, many line joints were connected in the way of CCP-IV; therefore, cracks directly coalesced on some joint planes due to the slide along the slant joint plane. The crack growth path was not analogous to that shown in Figs. 7c and 8c. In addition, some cracks propagated toward the adjacent joint plane, and the upper block may slide along the rupturing line

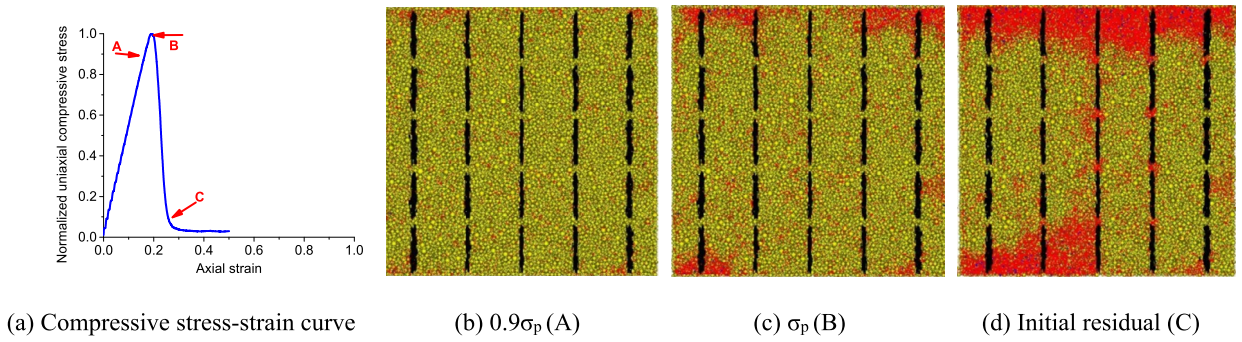


Fig. 10. Compressive failure process for sample 90-0.8.

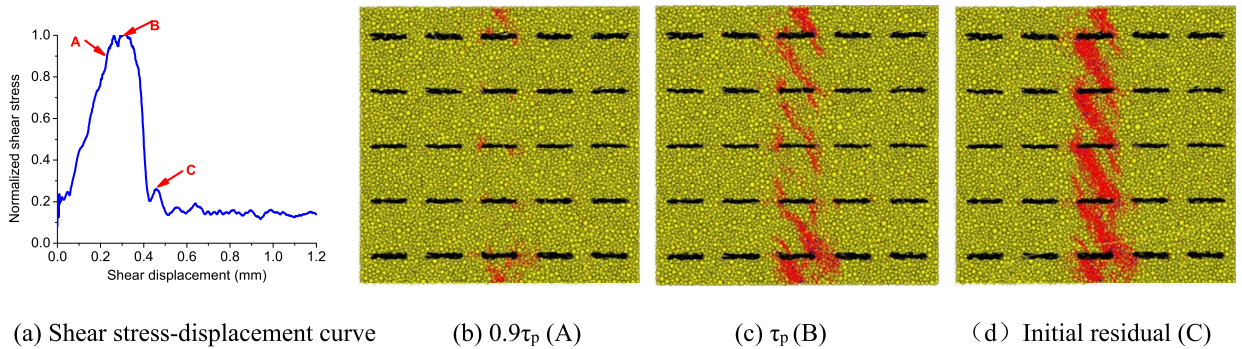


Fig. 11. Shear failure process for sample 0-0.4.

joint plane in the residual stage (see Fig. 9d). The failure process shown in Fig. 9 was observed in samples with high slant angles of 45°, 60°, and 75° except in sample 45-0.4. The failure process is called plane failure (compressive failure mode III, CFM-III).

Fig. 10 shows the compressive failure of sample 90-0.8. Referring to Fig. 10a, at $0.9\sigma_p$, micro-cracks were sporadically distributed in the sample as shown in Fig. 10b. Moreover, micro-cracks were yet to concentrate at the top and bottom ends of the sample close to the loading walls (see Fig. 10(c)). Unlike the aforementioned compressive failure process, no distinct crack initiation and propagation were observed at σ_p . After σ_p , due to lateral dilation under uniaxial compressive stress, dilation in the side direction caused some joint plane failures (see Fig. 10d). Given the concentration of compressive stress at sample ends, the 90° samples first failed at the ends. This failure behavior illustrated in Fig. 10 is called end compressive failure (compressive failure mode IV, CFM-IV), which only occurred in 90° samples.

Micro-cracks were mainly generated in the early stage of compressive loading. In most cases of compressive tests, crack initiation was not obvious before $0.9\sigma_p$ but mainly occurred after $0.9\sigma_p$. When $\alpha = 15^\circ, 30^\circ, \text{ and } 45^\circ$ ($k = 0.4$), crack initiation at the joint tip was easily observed. At the peak compressive stress, crack propagation became dramatic and some cracks coalesced. Although some cracks coalesced from $0.9\sigma_p$ to σ_p , cracks mainly coalesced after peak strength. According to the four types of failure processes, crack propagation and coalescence are largely depending on joint inclination. Four compressive failure modes were identified among all samples. Generally, samples with the same inclination angle, except for 45-0.4, exhibited the same failure mode.

3.3. Shear failure process

As shown in Fig. 5, a direct shear test was performed on the jointed samples with the same joint arrangement under compressive loading. Shear stress was normalized similar to the axial compressive stress. Similar to the compressive test, three loading points close to the peak shear stress (τ_p), $0.9\tau_p$, τ_p , and the initial residual moment, were selected to represent the shear failure process. Fig. 11 shows the shear failure process of sample 0-0.4. Referring to Fig. 11a, at $0.9\tau_p$, the crack initiated at the joint tips that intersected the shear plane and then propagated toward the adjacent joint tip in the same column. At τ_p , a few cracks coalesced between the vertical adjacent joints in the way of the CCP-III, but more cracks completely coalesced after τ_p . As shown in Figs. 11b–c, cracking only occurred in the column joints that intersected the shear plane and was barely observed in other column joints. This shear failure behavior was only observed in 0° and 45° samples, in which three or five joints were arranged in order across the shear plane. Shear load caused the crack to propagate near the shear plane. Given the difference between the joint inclination angles, the crack coalescence of the 45° sample was identified as CCP-II, whereas that of the 0° sample was CCP-IV. This shear failure process is called connecting

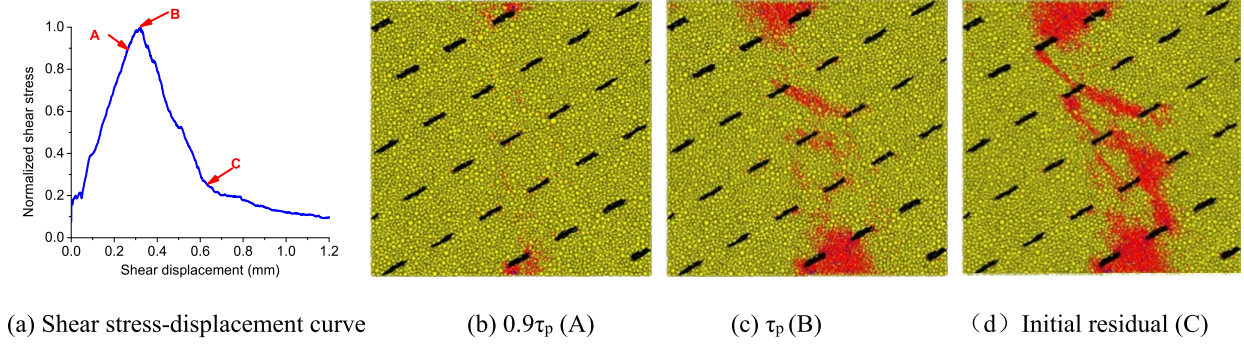


Fig. 12. Shear failure process for sample 30-0.4.

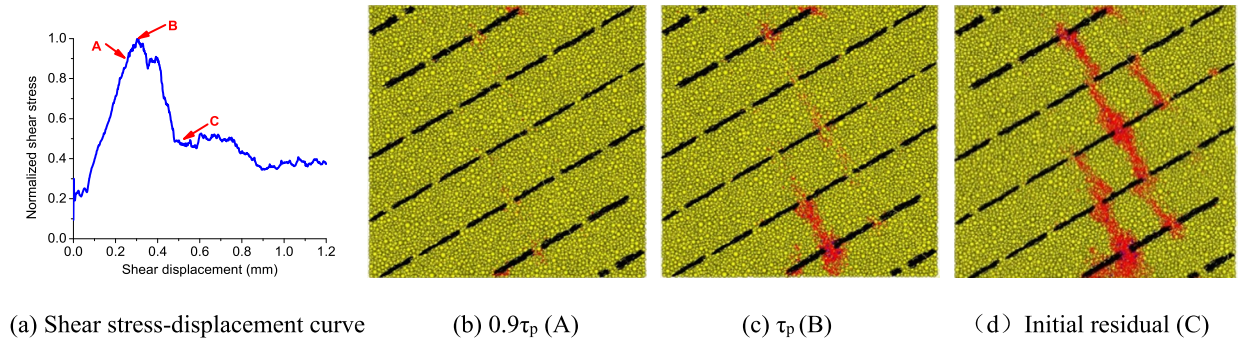


Fig. 13. Shear failure process for sample 60-0.8.

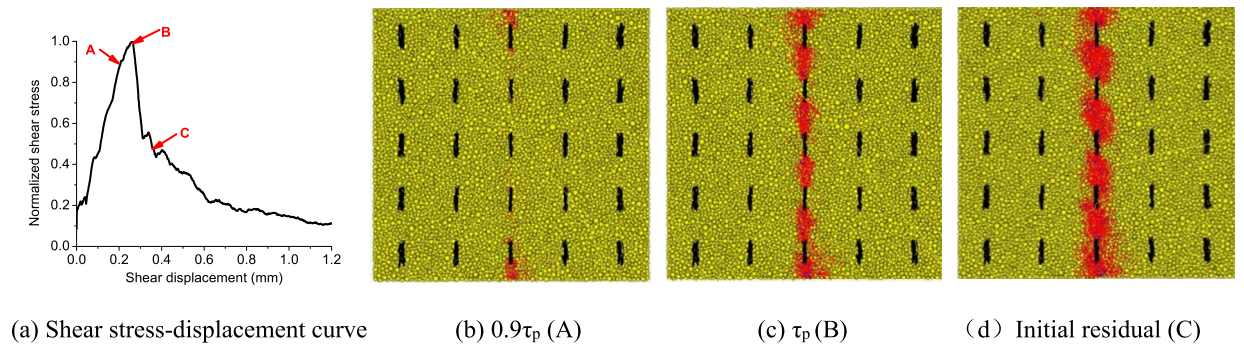


Fig. 14. Shear failure process for sample 90-0.4.

joint failure (shear failure mode I, SFM-I). The middle column joints were subjected to shear load; even if the shear load was applied across the midpoints of the middle column joints, cracks still initiated at the joint tips but not at the joint midpoint. In addition, no cracks occurred in the other column joints.

Fig. 12 shows the shear failure process of sample 30-0.4. Referring to Fig. 12(a), at $0.9\tau_p$, rupture initially occurred close to the loading wall, as shown in Fig. 12(b), and scattered micro-cracks were observed along the shear direction. At τ_p , one crack coalesced in the way of CCP-II. As loading continued, CCP-I, CCP-II, and CCP-III were observed at the point prior to the residual stage. Though the observed crack coalescence patterns were analogous to those shown in Fig. 8, the locations of cracking coalescence were different; that is, cracks coalesced close to the shear plane under shear loading, whereas cracks coalesced throughout the whole sample under compressive loading. The described shear failure process was mostly observed and mainly occurred in 15° , 30° , 60° , and 75° samples except for those with $k = 0.8$. Fig. 13 shows the shear failure process of sample 60-0.8. Referring to Fig. 13(a), at $0.9\tau_p$, rupture initially occurred at the initial loading point (Fig. 13(b)). At τ_p , cracks propagated approximately perpendicular to the joint plane (see Fig. 13(c)), i.e. in a column joint gap, and coalesced in the way shown in Fig. 13(d). When $k = 0.8$, the described failure process occurred in 15° , 30° , 45° , and 60° samples. The failure process shown in Figs. 12 and 13 is called non-shear plane failure (shear failure mode II, SFM-II).

Fig. 14 shows the shear failure process of sample 90-0.4. Combining the shear stress–shear displacement curve (Fig. 14a), as shown in Fig. 14b, shear failure initially occurred at two ends of the middle joint plane (see Fig. 14b). Furthermore, the

crack directly propagated along the shear plane and finally coalesced in the joint plane in the way of CCP-IV (see Figs. 14c and d). Given that the shear plane coincided with the middle joint plane, cracking only occurred on the shear plane. A high k value facilitated the failure process. The described failure was observed in 90° samples and sample 75-0.8. The failure process shown in Fig. 14 is called co-shear plane failure (shear failure mode III, SFM-III).

Cracking was not obvious during the early stage of shear loading. Cracks only occurred near or along the shear plane in 0°, 45°, and 90° samples. For other samples, cracks ran through the column joint gaps. Three shear failure modes were identified based on the cracking location. Although joint arrangements were the same, cracking processes were different under compressive and shear loading due to different loading processes. Rupture occurred within the whole sample under compressive loading and close to the shear plane under shear loading. An accessional compressive effect existed under shear loading; thus, some cracking growths like those under compressive loading were observed; for instance, that shown in Figs. 12 and 13. The angle between the shear loading direction and the joint plane differed from that between compressive loading direction and joint plane. The difference between compressive and shear failure will be compared in the following section.

3.4. Comparison of shear and compressive failure

The compressive and shear failure processes of samples with the same joint arrangement are different. Usually, the compressive or shear failure modes of the samples with identical slant angles are the same. Thus, one failure case for $\alpha = 0^\circ, 15^\circ, 30^\circ, 60^\circ,$ and 90° and two failure cases for $\alpha = 45^\circ$ and 75° were selected for the comparison of final compressive and shear failure. As shown in Figs. 15a1 and a2, when $\alpha = 0^\circ$, the loading direction was perpendicular to the joint plane, and the compressive and failure processes were completely different. Crack initiation and propagation occurred at most joints under compressive loading, but occurred only at the middle column joints under shear loading. The crack coalescence patterns were also different. CCP-I and CCP-II were observed during compressive failure, whereas CCP-III was the only coalescence pattern observed during shear failure. As shown in Figs. 15(b1) and (b2), when $\alpha = 15^\circ$, CCP-I and CCP-II were observed during compressive and shear failure; however, more cracks were generated during compressive failure than during shear and cracking locations varied. When $\alpha = 30^\circ$, CCP-I, CCP-II, and CCP-III were all observed during compressive and shear failure as listed in Table 3. Although cracking locations varied, however, the crack growth path was similar, as shown in Figs. 15c1 and c2. When $\alpha = 45^\circ$, the compressive failure mode for sample 45-0.4 differed from those of samples 45-0.6 and 45-0.8; in contrast, the shear failure mode was the same for all 45° samples, just like 0° samples. Cracking pattern during compressive and shear failure were different, just like 0° samples. Compressive failure in sample 45-0.4 resulted from CCP-III and from CCP-IV in samples 45-0.6 and 45-0.8. In 45° samples, shear failure resulted from CCP-II (see Figs. 15d1 and d2, and Figs. 15e1 and e2). When $\alpha = 60^\circ$, the sample slides along the line joint plane under compressive stress and failed in CFM-III. Under shear load, the crack grew across the joint planes; however, the combination of joint and crack did not completely run through the sample. As shown in Figs. 15f1 and f2, the crack growth paths were completely different in compressive and shear failure. When $\alpha = 75^\circ$, compressive failure extended along the joint plane for samples with different continuity factors (Fig. 15g1); on the contrary, for samples 75-0.4 and 75-0.6, the shear failure shown in Fig. 15g2 resulted from CCP-II and CCP-III. For sample 75-0.8, as shown in Figs. 15(h1) and (h2), failure occurred along the joint plane under compressive and shear loading due to the small angle between the loading direction and joint plane, and the short distance between adjacent joints on same plane. When $\alpha = 90^\circ$, under uniaxial compression, the sample dilated in the side direction, and joints on the same joint plane connected with each other (Fig. 15i1). Basically, the joint-connecting behavior may occur on several joint planes. But under direct shear load, shear failure merely occurred on the middle joint plane (Fig. 15i2), i.e. the sample was cut into the upper and lower blocks along the middle joint plane. The upper block slides along the failure plane. In the previous studies, although the joint arrangement was the same, compressive and shear failure differed in (a) crack number and location and (b) crack coalescence patterns. In (a), cracks were generated at any location under compressive loading, whereas cracks were close to the shear plane under shear loading, particularly when the angle between the joint plane and shear direction was very small, for example, in 75-0.8 and 90° samples. The whole sample cross section was subjected to stress under compressive loading, whereas the shear plane was subjected to shear stress and an accessional stress from the loading wall. In (b), crack coalescence patterns were completely different for 0°, 45°, and 75° samples except for sample 75-0.8. However, the crack coalescence patterns were the same or similar for 15°, 30°, 60°, and 90° samples under compressive and shear loading.

3.5. Contact force evolution during compressive and shear loading process

In the PFC model, due to particles movement under outside loading, a force exists on the bond between particles. This force is called contact force. The contact force is represented using short lines. Before loading, the contact force is uniformly distributed within samples but changes during loading. In this section, the evolution of the contact force during typical failure processes under compressive and shear loading is analyzed. The contact force at four critical moments—before loading, 50% of peak strength ($0.5\sigma_p$ or $0.5\tau_p$), peak strength (σ_p or τ_p), and the point reaching the residual stage—represents the changes during the entirety of the loading process.

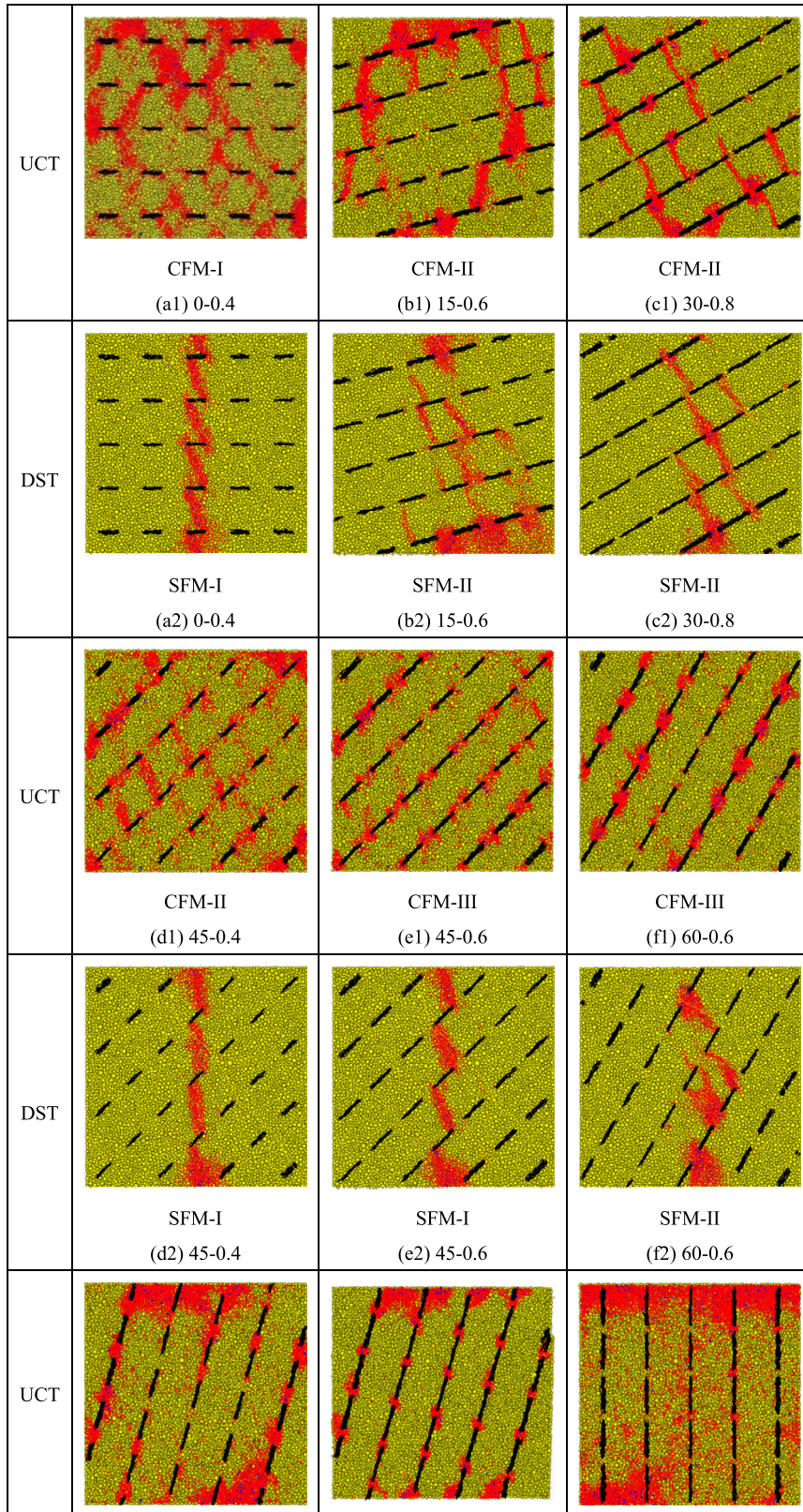


Fig. 15. Comparison of final failure status under compressive and shear loading.

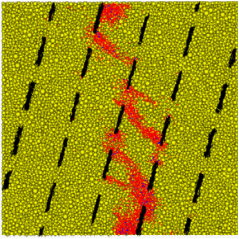
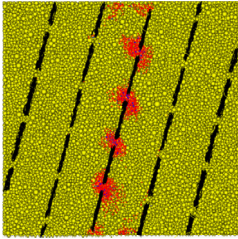
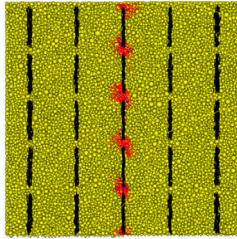
	CFM-III (g1) 75-0.6	CFM-III (h1) 75-0.8	CFM-IV (i1) 90-0.8
DST			
	SFM-II (g2) 75-0.6	SFM-III (h2) 75-0.8	SFM-III (i2) 90-0.8

Fig. 15. (continued)

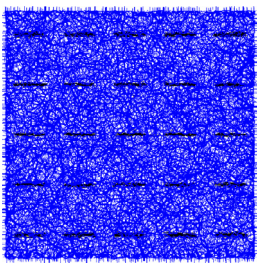
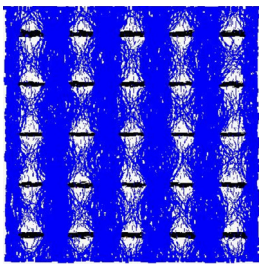
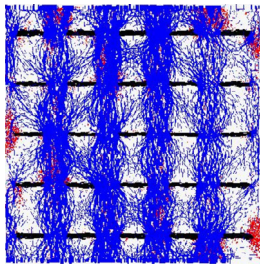
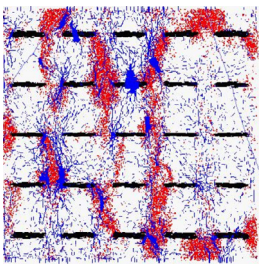
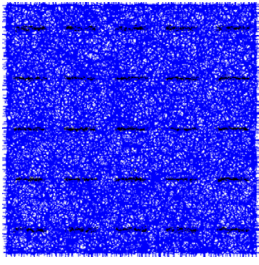
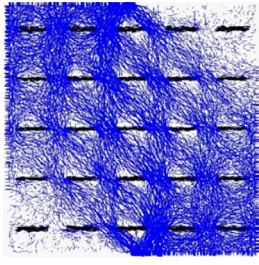
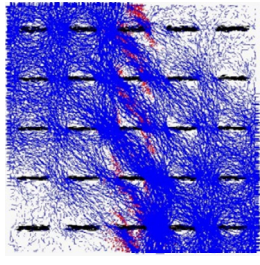
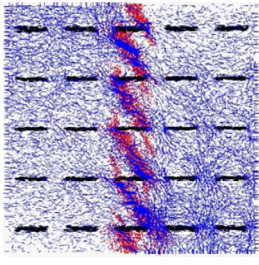
CFM-I				
	(a1) Before loading	(b1) $0.5\sigma_p$	(c1) σ_p	(d1) Initial residual
SFM-I				
	(a2) Before loading	(b2) $0.5\tau_p$	(c2) τ_p	(d2) Initial residual

Fig. 16. Contact force evolution during compressive and shear loading for sample 0-0.6.

Fig. 16 shows the contact force evolution of sample 0-0.6 under compressive and shear loading. As mentioned above and as shown in Figs. 16a1 and a2 and Figs. 17 to 19, regardless of compressive or shear load, the contact force was uniformly distributed before loading. When loaded at $0.5\sigma_p$ or $0.5\tau_p$, the contact force was gradually and intensively distributed, as shown in Figs. 16b1 and b2. The contact force distribution under compressive or shear loading was distinctly different. A contact force was applied in the column joint gaps under compression but localized at line joint ligaments on the same plane and close to the loading walls where shear failure first occurred. Referring to Fig. 5, W_5 and W_8 compressed the particle assembly and the contact force was concentrated near the two walls. However, the contact force never concentrated near W_6 and W_7 . This phenomenon was observed for all samples under shear loading. At peak strength, the contact force under compression shown in Fig. 16c1 becomes scattered relative to Fig. 16b1; at this point, some cracks propagated, whereas others coalesced. Under shear loading, the contact force is mainly concentrated close to the shear plane (Fig. 16c2) and cracks were extensively created as shown in Fig. 11c. Cracks occurred where the contact force was mostly concentrated. At an initial residual point, the contact force was scattered except at some joint ligaments due to crack coalescence (see Figs. 16d1 and d2).

Fig. 17 shows the contact force evolution of sample 30-0.4 during compressive and shear failure. The contact force distribution in this sample was identical to that in sample 0-0.6 before loading (see Figs. 18a1 and a2). The same rule was found for all samples and will not be repeatedly described. Under $0.5\sigma_p$ or $0.5\tau_p$, the contact force was distributed nearly

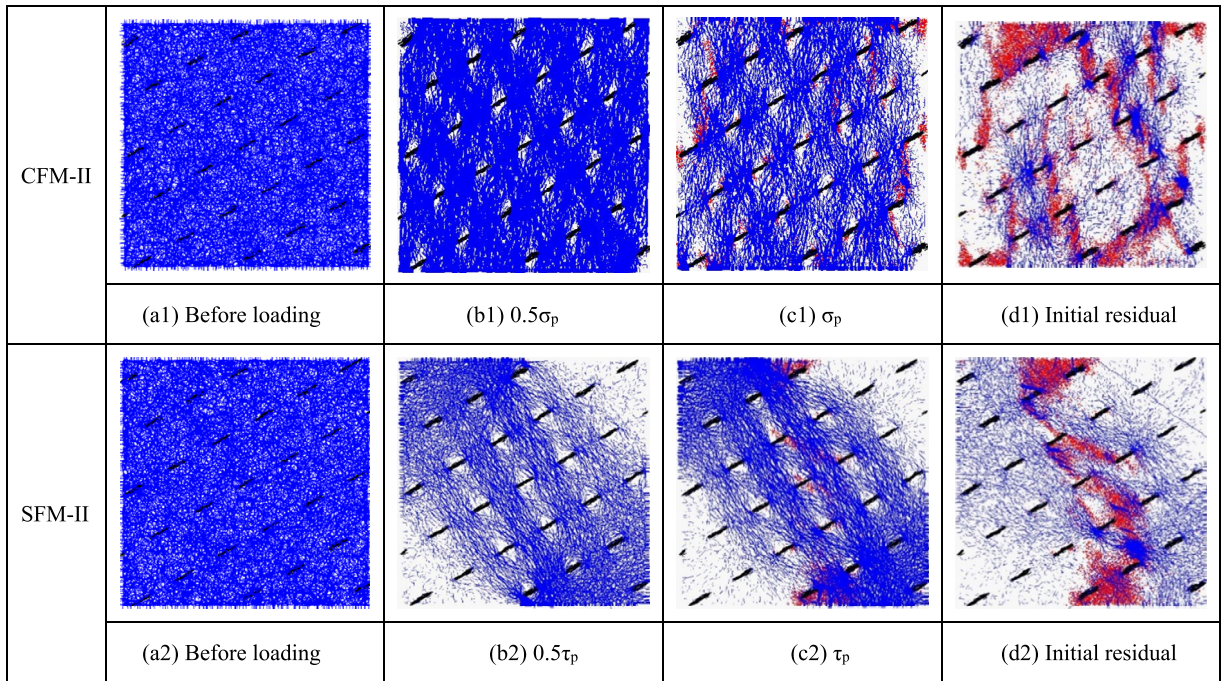


Fig. 17. Contact force evolution during compressive and shear loading for sample 30-0.4.

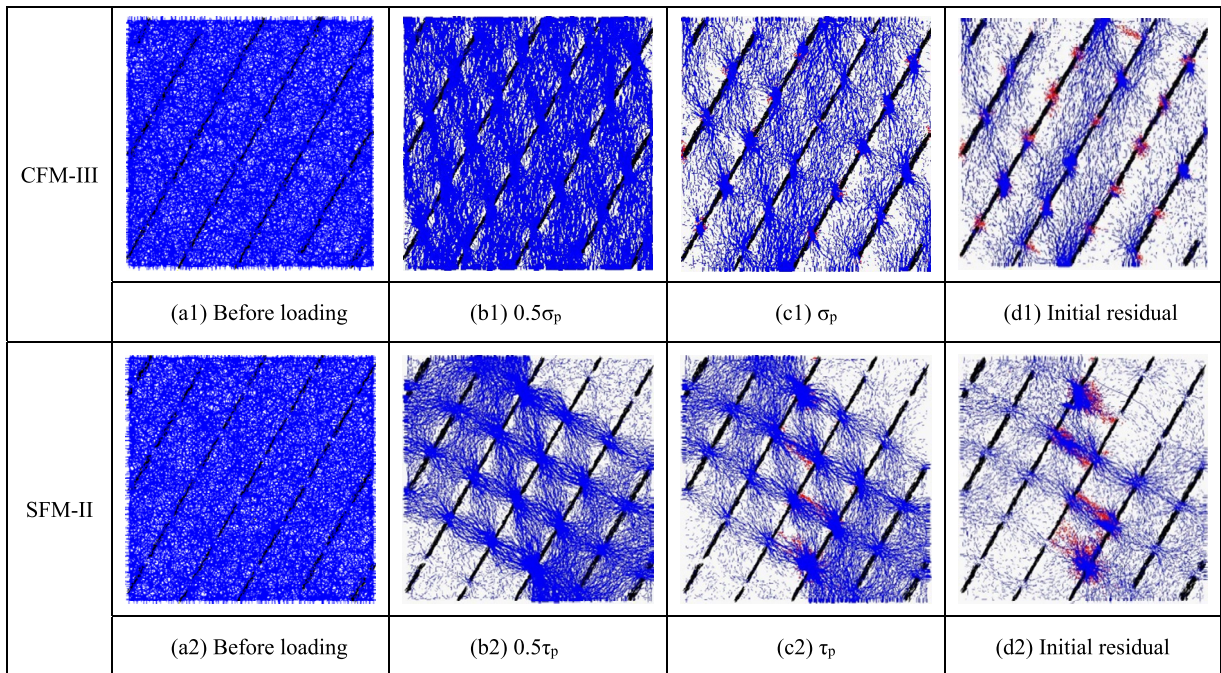


Fig. 18. Contact force evolution during compressive and shear loading for sample 60-0.8.

around all joint tips in the compressive case, whereas contact forces in shear are mainly distributed close to the loading walls and in the gaps between joint columns (see Figs. 17b1 and b2). At this moment, the crack was hardly initiated. At peak strength, the contact force was still concentrated at joint tips, but the degree of concentration became less intensive (see Figs. 17c1 and c2). Cracking occurred at the location where the contact force was concentrated. As cracking continued, the contact force became scattered (see Figs. 17d1 and d2).

Fig. 18 shows the contact force evolution of sample 60-0.8 under compressive and shear loading. At $0.5\sigma_p$ or $0.5\tau_p$, the contact force was distributed at joint tips under compressive loading, as shown in Fig. 18b1, and at the joint ligaments in the

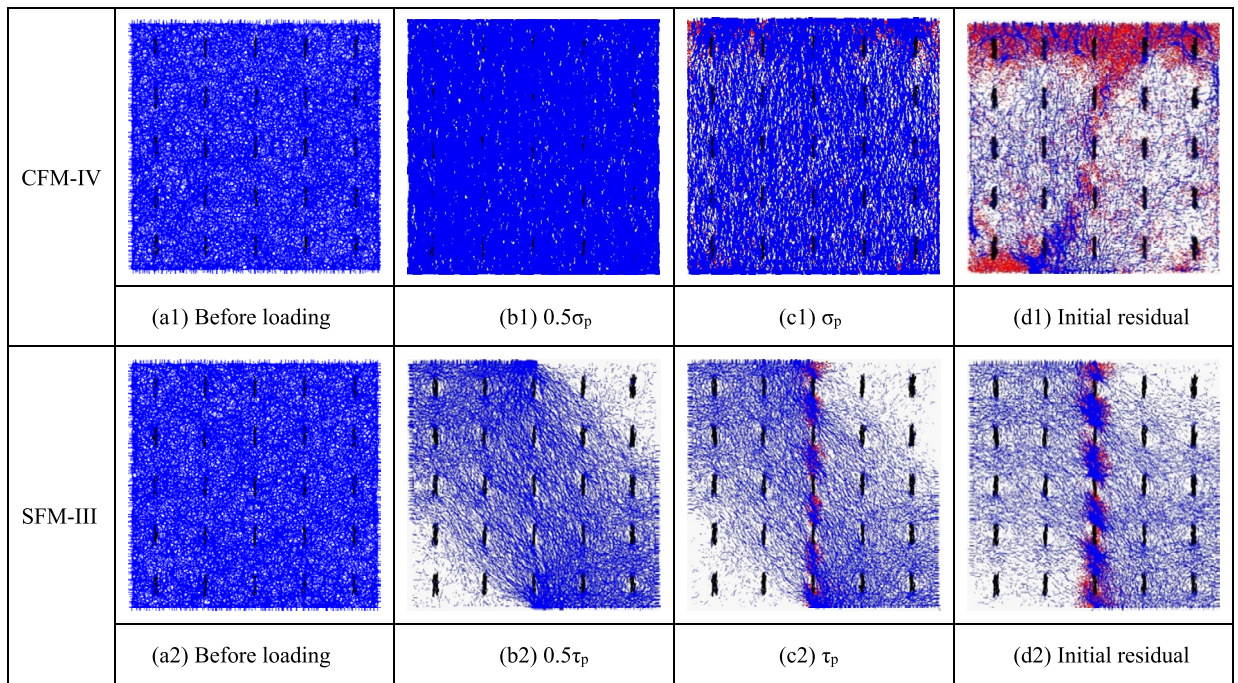


Fig. 19. Contact force evolution during compressive and shear loading for sample 90-0.4.

joint plane under shear loading, as shown in Fig. 18b2. At peak strength, contact force under compression was concentrated in the line joint gaps (Figs. 18c1 and c2); therefore, cracks coalesced on the joint plane. This change accounted for the plane failure shown in Figs. 9c and 15e1–h1. Under shear loading, the contact force was concentrated at line and column joint ligaments. This change corresponds to the shear failure shown in Fig. 13d. At the initial residual moment, the contact force became scattered under compressive and shear loading (Figs. 18d1 and d2).

Fig. 19 shows the contact force evolution of sample 90-0.4. At $0.5\sigma_p$ or $0.5\tau_p$, the contact force distributed under compressive (see Fig. 19b1) loading was different from that under shear loading (see Fig. 19b2). Moreover, the contact force differed from that described above. Under compressive loading, the contact force was not distributed at the joint tips, but nearly throughout the whole sample. At and after peak strength, the contact force was distributed close to the loading wall to some degree (Figs. 19c1 and c2). This situation accounted for the rupture of sample ends shown in Fig. 10c. At $0.5\tau_p$, the contact force was not concentrated at joint tips. This distribution was vastly different from that described in samples under shear loading. From τ_p to the initial residual moment, the contact force was intensively distributed along the shear plane, as shown in Figs. 19c2 and d2. This distribution pattern accounted for failure along the shear plane, as shown in Fig. 14b.

Contact force distribution varied due to different loading methods. The contact force concentration location was related to the loading method and joint arrangement. Usually, the contact force was concentrated at the joint ligament. Cracks initiated and propagated at the location of contact force concentration. Contact force evolution was completely different under compressive and shear loading. The contact force was partially concentrated under shear loading, especially close to the shear plane, but concentrated in the whole jointed sample under compressive loading. Regardless of whether under compressive or shear loading, the contact force distribution was uniform before loading, then concentrated, and finally scattered after failure.

4. Conclusions

(1) Four crack coalescence patterns were observed during compressive and shear tests. Generally, each sample exhibited one or two crack coalescence patterns. Three crack coalescence patterns were observed in some samples, such as in 30-0.4 and 30-0.6 under compressive loading and in 75-0.6 under shear loading. The pattern of crack coalescence was mainly related to the joint inclination angle. In most cases, the observed crack coalescence patterns under compressive loading were different from those under shear loading. The same crack coalescence pattern was observed in the 30° and 90° samples.

(2) Four compressive failure modes, namely, vertical cleavage, slant cleavage, plane, and end compressive, were identified. Failure modes were closely related to the joint inclination angle; generally, samples with equivalent slant angles failed in the same mode except for sample 45-0.4. A high k value facilitated compression failure in samples with the same slant angle

(3) Three shear failure modes, namely, connecting joint intersecting shear plane, non-shear plane, and co-shear plane, were identified. Shear failure modes were associated with joint arrangement on the shear plane. A small angle between shear direction and joint increases the shear failure rate. A high k value facilitated shear failure with the same slant angle.

(4) Comparing compressive and shear failure revealed that both loading methods differed in terms of cracking location and number of cracks. More cracks and cracking locations were generated in compressive failure than in shear failure. All samples failed in different modes except for sample 75-0.8, which failed along the joint plane in compressive and shear failure.

(5) Irrespective of whether under compressive or shear loading, the contact force exhibited three stages: uniform distribution before loading, concentrated distribution, and scattered distribution after failure. All samples exhibited different contact force evolution patterns under compressive and shear loading. The concentrated locations of the contact force were related to the loading method and the joint configuration.

Acknowledgements

This paper gets its funding from the following projects: Projects 51774322, 41807241, 41562016, supported by the National Natural Science Foundation of China; Project kfj170406, supported by the Open Fund of Engineering Research Center of Catastrophic Prophylaxis and Treatment of Road & Traffic Safety of Ministry of Education (Changsha University of Science & Technology); Project 2018JJ2500, supported by the Hunan Provincial Natural Science Foundation of China; Project 2016019, supported by the Research Fund of Department of Transportation of Zhejiang Province; Project 2017-1-4 supported by the Traffic Construction Research Fund of Shanxi Province; Project 2018JQ4015, supported by the Natural Science Basic Research Plan of Shaanxi Province (China). The authors wish to acknowledge these supports.

References

- [1] Q. Lin, P. Cao, R. Cao, Experimental investigation of jointed rock breaking under a disc cutter with different confining stresses, *C. R. Mecanique* 346 (2018) 833–843.
- [2] A. Carpinteri, G. Fortese, C. Ronchei, D. Scorza, S. Vantadori, Mode I fracture toughness of fibre reinforced concrete, *Theor. Appl. Fract. Mech.* 91 (2017) 66–75.
- [3] L. Liu, Z. Fang, C. Qi, B. Zhang, L. Guo, K. Song, Numerical study on the pipe flow characteristics of the cemented paste backfill slurry considering hydration effects, *Powder Technol.* 343 (2019) 454–464.
- [4] J. Justo, J. Castro, S. Cicero, M. Sánchez-Carro, R. Husillos, Notch effect on the fracture of several rocks: application of the theory of critical distances, *Theor. Appl. Fract. Mech.* 90 (2017) 251–258.
- [5] H. Lin, P. Cao, Y. Wang, Numerical simulation of a layered rock under triaxial compression, *Int. J. Rock Mech. Min. Sci.* 60 (2013) 12–18.
- [6] Y. Liu, F. Dai, L. Dong, N. Xu, P. Feng, Experimental investigation on the fatigue mechanical properties of intermittently jointed rock models under cyclic uniaxial compression with different loading parameters, *Rock Mech. Rock Eng.* 51 (2018) 47–68.
- [7] S.Q. Yang, Experimental study on deformation, peak strength and crack damage behavior of hollow sandstone under conventional triaxial compression, *Eng. Geol.* 213 (2016) 11–24.
- [8] X.P. Zhang, L.N.Y. Wong, Crack initiation, propagation and coalescence in rock-like material containing two flaws: a numerical study based on bonded-particle model approach, *Rock Mech. Rock Eng.* 46 (2013) 1001–1021.
- [9] X. Chen, Z. Liao, X. Peng, Deformability characteristics of jointed rock masses under uniaxial compression, *Int. J. Min. Sci. Technol.* 22 (2012) 213–221.
- [10] R. Cao, P. Cao, H. Lin, G. Ma, Y. Chen, Failure characteristics of intermittent fissures under a compressive-shear test: experimental and numerical analyses, *Theor. Appl. Fract. Mec.* 96 (2018) 740–757.
- [11] N. Xu, F. Dai, C. Sha, Y. Lei, B. Li, Microseismic signal characterization and numerical simulation of concrete beam subjected to three-point bending fracture, *J. Sensors* 2015 (2015) 987232, 11 p.
- [12] L.N.Y. Wong, H.H. Einstein, Crack coalescence in molded gypsum and carrara marble, part 1: macroscopic observations and interpretation, *Rock Mech. Rock Eng.* 42 (2009) 475–511.
- [13] M. Sagong, A. Bobet, Coalescence of multiple flaws in a rock-model material in uniaxial compression, *Int. J. Rock Mech. Min. Sci.* 39 (2002) 229–241.
- [14] Y. Zhao, L. Zhang, W. Wang, J. Tang, H. Lin, Transient pulse test and morphological analysis of single rock fractures, *Int. J. Rock Mech. Min. Sci.* 91 (2017) 139–154.
- [15] X. Fan, K. Li, H. Lai, Y. Xie, R. Cao, J. Zheng, Internal stress distribution and cracking around flaws and openings of rock block under uniaxial compression: a particle mechanics approach, *Comput. Geotech.* 102 (2018) 28–38.
- [16] X. Fan, R. Chen, H. Lin, H. Lai, C. Zhang, Q. Zhao, Cracking and failure in rock specimen containing combined flaw and hole under uniaxial compression, *Adv. Civ. Eng.* 2018 (2018) 9818250, <https://doi.org/10.1155/2018/9818250>.
- [17] X.P. Zhang, L.N.Y. Wong, S. Wang, Effects of the ratio of flaw size to specimen size on cracking behavior, *Bull. Eng. Geol. Environ.* 74 (2016) 181–193.
- [18] C.A. Tang, S.Q. Kou, Crack propagation and coalescence in brittle materials under compression, *Eng. Fract. Mech.* 61 (1998) 311–324.
- [19] M. Jiang, C. Sun, A. Rodriguezdono, N. Zhang, J. Shao, Influence of time-dependence on failure of echelon rock joints through a novel DEM model, *Eur. J. Environ. Civ. Eng.* 19 (2015) s108–s118.
- [20] Y. Zhao, Y. Wang, W. Wang, W. Wan, J. Tang, Modeling of non-linear rheological behavior of hard rock using triaxial rheological experiment, *Int. J. Rock Mech. Min. Sci.* 93 (2017) 66–75.
- [21] S.Q. Yang, Y.Z. Jiang, W.Y. Xu, X.Q. Chen, Experimental investigation on strength and failure behavior of pre-cracked marble under conventional triaxial compression, *Int. J. Solids Struct.* 45 (2008) 4796–4819.
- [22] L.N.Y. Wong, H.Q. Li, Numerical study on coalescence of two pre-existing coplanar flaws in rock, *Int. J. Solids Struct.* 50 (2013) 3685–3706.
- [23] X. Chen, Z. Liao, X. Peng, Cracking process of rock mass models under uniaxial compression, *J. Cent. South Univ. Technol.* 20 (2013) 1661–1678.
- [24] A. Bobet, H.H. Einstein, Fracture coalescence in rock-type materials under uniaxial and biaxial compression, *Int. J. Rock Mech. Min. Sci.* 35 (1998) 863–888.
- [25] P. Lin, R.H.C. Wong, K.T. Chau, C.A. Tang, Multicrack coalescence in rock-like material under uniaxial and biaxial loading, *Key Eng. Mater.* 183–187 (2000) 809–814.
- [26] P.H.S.W. Kulatilake, W. He, J. Um, H. Wang, A physical model study of jointed rock mass strength under uniaxial compressive loading, *Int. J. Rock Mech. Min. Sci.* 34 (1997) 165.e1–165.e15.

- [27] M. Prudencio, M.V.S. Jan, Strength and failure modes of rock mass models with non-persistent joints, *Int. J. Rock Mech. Min. Sci.* 44 (2007) 890–902.
- [28] M. Bahaaddini, G. Sharrock, B.K. Hebblewhite, Numerical investigation of the effect of joint geometrical parameters on the mechanical properties of a non-persistent jointed rock mass under uniaxial compression, *Comput. Geotech.* 49 (2013) 206–225.
- [29] H. Lin, W. Xiong, Q. Yan, Three-dimensional effect of tensile strength in the standard Brazilian test considering contact length, *Geotech. Test. J.* 39 (2016) 137–143.
- [30] H. Lin, W. Xiong, Q. Yan, Modified formula for the tensile strength as obtained by the flattened Brazilian disk test, *Rock Mech. Rock Eng.* 49 (2016) 1579–1586.
- [31] X. Fan, K.H. Li, H.L. Lai, Q.H. Zhao, Z.H. Sun, Experimental and numerical study of the failure behavior of intermittent rock joints subjected to direct shear load, *Adv. Civ. Eng.* 2018 (2018) 4294501, <https://doi.org/10.1155/2018/4294501>, 19 p.
- [32] P.K. Kaiser, C.A. Tang, Numerical simulation of damage accumulation and seismic energy release during brittle rock failure, part II: rib pillar collapse, *Int. J. Rock Mech. Min. Sci.* 35 (1998) 123–134.
- [33] X. Fan, P.H.S.W. Kulatilake, X. Chen, P. Cao, Crack initiation stress and strain of jointed rock containing multi-cracks under uniaxial compressive loading: a particle flow code approach, *J. Cent. South Univ. Technol.* 22 (2015) 638–645.
- [34] R.H. Cao, P. Cao, X. Fan, X. Xiong, H. Lin, An experimental and numerical study on mechanical behavior of ubiquitous-joint brittle rock-like specimens under uniaxial compression, *Rock Mech. Rock Eng.* 49 (2016) 4319–4338.
- [35] X. Fan, P.H.S.W. Kulatilake, X. Chen, Mechanical behavior of rock-like jointed blocks with multi-non-persistent joints under uniaxial loading: a particle mechanics approach, *Eng. Geol.* 190 (2015) 17–32.
- [36] H. Lin, H. Wang, X. Fan, P. Cao, K. Zhou, Particle size distribution effects on deformation properties of graded aggregate base under cyclic loading, *Eur. J. Environ. Civ. Eng.* (2016), <https://doi.org/10.1080/19648189.2016.1276480>.
- [37] Z. He, B. Wang, Instability process model test for bedding rock slope with weak interlayer under different rainfall conditions, *Adv. Civ. Eng.* 2018 (2018) 8201031, 8 p.
- [38] X.P. Zhang, L.N.Y. Wong, Cracking processes in rock-like material containing a single flaw under uniaxial compression: a numerical study based on parallel bonded-particle model approach, *Rock Mech. Rock Eng.* 45 (2012) 711–737.
- [39] Z.C. Kang, Q. Liu, J. Huang, New criterion for rock joints based on three-dimensional roughness parameters, *J. Cent. South Univ. Technol.* 21 (2014) 4653–4659.
- [40] M. Bahaaddini, Effect of boundary condition on the shear behaviour of rock joints in the direct shear test, *Rock Mech. Rock Eng.* 50 (2017) 1141–1155.
- [41] C.C. Xia, Z.C. Tang, W.M. Xiao, Y.L. Song, New peak shear strength criterion of rock joints based on quantified surface description, *Rock Mech. Rock Eng.* 47 (2014) 387–400.
- [42] M.S. Asadi, V. Rasouli, G. Barla, A bonded particle model simulation of shear strength and asperity degradation for rough rock fractures, *Rock Mech. Rock Eng.* 45 (2012) 649–675.
- [43] G. Grasselli, P. Egger, Constitutive law for the shear strength of rock joints based on three-dimensional surface parameters, *Int. J. Rock Mech. Min. Sci.* 40 (2003) 25–40.
- [44] E. Gerolymatou, T. Triantafyllidis, Shearing of materials with intermittent joints, *Rock Mech. Rock Eng.* 49 (2016) 1–12.
- [45] A. Ghazvinian, V. Sarfarazi, W. Schubert, M. Blumel, A study of the failure mechanism of planar non-persistent open joints using PFC2D, *Rock Mech. Rock Eng.* 45 (2012) 677–693.
- [46] C. Gehle, H.K. Kutter, Breakage and shear behaviour of intermittent rock joints, *Int. J. Rock Mech. Min. Sci.* 40 (2003) 687–700.
- [47] H.Q. Zhang, Z.Y. Zhao, C.A. Tang, L. Song, Numerical study of shear behavior of intermittent rock joints with different geometrical parameters, *Int. J. Rock Mech. Min. Sci.* 43 (2006) 802–816.
- [48] S. Liu, H. Liu, S. Wang, B. Hu, X. Zhang, Direct shear tests and PFC2D numerical simulation of intermittent joints, *Chin. J. Rock Mech. Eng.* 27 (2008) 1828–1836.
- [49] Itasca Consulting Group, PFC3D User's Manual, Itasca Consulting Group, Minneapolis, MN, USA, 2003.